analytical chemistry

pubs.acs.org/ac Article

Tunable Competitive Absorption-Induced Signal-On Photoelectrochemical Immunoassay for Cardiac Troponin I Based on Z-Scheme Metal−Organic Framework Heterojunctions

Yuan Gao, Meijin Li,* Yongyi Zeng, Xiaolong Liu, and Dianping Tang*

Cite This: *Anal. Chem.* 2022, 94, 13582−13589 Read Online

ACCESS | Metrics & More | Article Recommendations | Supporting Information

ABSTRACT: Recently emerged Z-scheme heterostructure-based immunoassays have presented new opportunities for photoelectrochemical (PEC) biosensing development. Here, we described a tunable signal-on PEC biosensor for the detection of cardiac troponin I (cTnI), which exploited a competitive absorption effect between Cu(II) ions and a Zr metal−organic framework (Zr-MOF) constructed on TiO_2 nanorods (Cu^{2+}@Zr-MOF@TiO_2 NRs). Water-stable Zr-MOF was coated onto TiO_2 NRs on fluorine-doped tin oxide to form a Z-scheme heterostructure substrate (Zr-MOF@TiO_2 NRs), which exhibited a high photoelectric response. Cu^{2+}@Zr-MOF@TiO_2 NRs, constructed by loading Cu(II) ions onto the architecture of Zr-MOF by electrostatic interaction, demonstrated a low background signal. After sandwich immunorecognition within a 96-well plate, H_2S, generated by confined alkaline phosphatase on zeolitic imidazolate framework-8, was directed to react with Cu(II) ions to form CuS. This resulted in an in situ change in the photoelectrode and an enhanced photoelectric signal. The developed PEC biosensing platform exhibited high sensitivity and selectivity for the cTnI immunoassay with a detection limit of 8.6 pg/mL. The Z-scheme-based competition absorption modulation of photoelectrochemistry provides a new strategy for general PEC biosensing development.

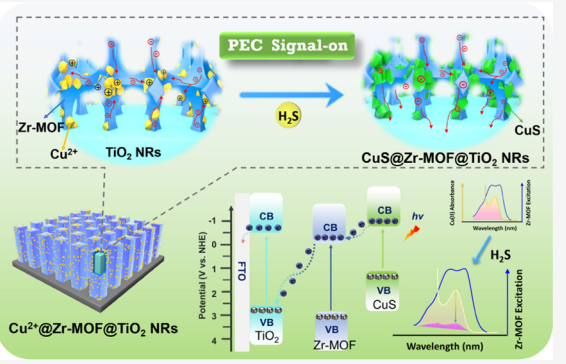

Acute myocardial infarction (AMI) is the most common form of cardiovascular disease, representing a high mortality rate globally. The general diagnosis of AMI in clinical practice requires the comprehensive consideration of an electrocardiogram and abnormal biomarker levels. Evidence from the scientific literature has revealed that cardiac biomarkers, e.g., myoglobin, B-type natriuretic peptide, heart-type fatty acid binding protein (h-FABP), and cardiac troponin I (cTnI), can provide a rapid diagnosis of AMI.[1−5] However, detection of the extremely small variations in the concentrations of these biomarkers during the onset of AMI remains challenging, which limits accurate diagnosis. Several techniques have been proposed for the analysis of AMI biomarkers including fluorescence,[6,7] chemiluminescence,[8] photothermal biosensing,[9,10] and electrochemical detection.[11−13] Among these, advanced photoelectrochemical (PEC) bioanalysis enables the fusion of photodriven electrochemical responses with various biological recognition events to monitor physiological and pathological parameters, making it a promising and burgeoning technique in life science research.[14−16] Currently, developing unique signal-on sensing mechanisms is a significant research branch in PEC bioanalysis due to their reduced background signals and high sensitivity. Therefore, the development of a signal-on amplified PEC bioanalysis for AMI biomarker detection is highly desirable.

Metal−organic frameworks (MOFs) are porous hybrid materials composed of different inorganic metal clusters/ions coordinated by organic linkers.[17] The high surface areas and controllable surface functionalization of MOFs have broadened their range of applications, e.g., in catalysis, sensing, gas storage, and separation.[18] Recently, MOFs incorporating metal clusters, such as ZIF-8, PCN-224, and HKUST-1, have been used for PEC detection. For example, MOF-based composites have been functionalized by hybridizing with photoactive semiconductors or metal nanoparticles, calcining to the corresponding metal oxides, conjugating with enzymes as signal labels, etc.[19−24] Wu et al. decorated Au/UiO-66(NH_2) with CdS to improve visible-light harvesting efficiency and biocompatibility for the detection of diethylstilbestrol.[25] Zhang et al. calcined Fe-based MOFs to synthesize porous magnetic Fe_3O_4 octahedra prior to loading with CdS via successive ionic layer adsorption to develop a microRNA bioassay method.[26] Constructing Z-scheme heterojunctions has been realized as a

Received: July 27, 2022
Accepted: September 9, 2022
Published: September 21, 2022

https://doi.org/10.1021/acs.analchem.2c03263
Anal. Chem. 2022, 94, 13582−13589

Scheme 1. Schematic Illustration of the Signal-On PEC Immunoassay Based on the Tunable Competitive Absorption of Cu(II) Ions onto a MOF-Based Heterojunction

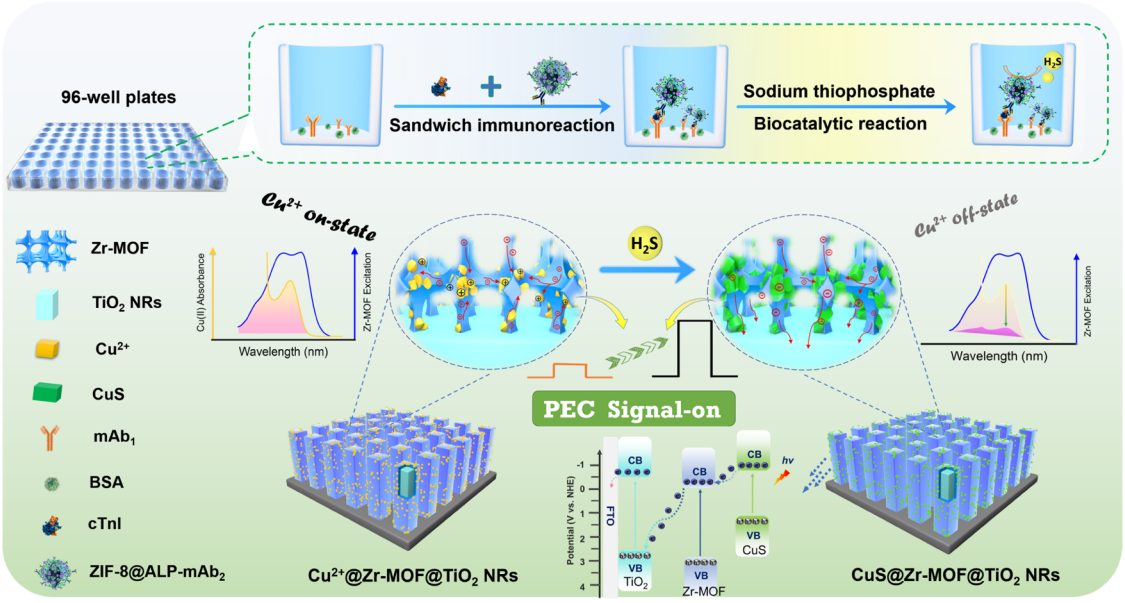

forward-looking way to prepare photoactive materials in PEC biosensing due to the advantages of effective spatial separation of photogenerated electron−hole pairs and unique charge migration pathways. Although MOF-based heterojunctions have been developed, application of the equivalent Z-scheme heterojunctions to the PEC bioanalysis of various biomarkers has received little attention.

The tunable structural and functional properties of MOFs have extended the range of biosensing mechanisms in combination with the physiochemical parameters of targeted analytes. For example, the strong absorption competition of guests may inhibit the inherent excitation energy of MOF-based complexes, leading to luminescence quenching. When an overlap occurs between the excitation spectra of MOF-based composites and the UV−vis absorption spectra of a guest, competitive absorption for the input light may happen, resulting in the ineffective excitation of MOF-based materials.[27] Recently, this mechanism has been used in fluorescence sensing. Hu et al. prepared a two-dimensional MOF-nanosheet luminescent probe to detect Fe^{3+} ions based on competitive light absorption and electron transfer between the ligand moieties and Fe^{3+} ions.[28] Xu et al. designed a fluorescent nanosensor for the detection of alkaline phosphatase (ALP) based on Zr-MOF and the catalyzed products of disodium *p*-nitrophenyl phosphate via a competitive absorption mechanism.[29] However, the PEC biosensing strategy based on competitive absorption is still in its infancy.[30] Hence, the aim of this study was to combine the competitive absorption of excited light resources to engineer an advanced signal-on PEC immunoassay.

Inspired by the competitive absorption mechanism, a strategy has been developed to introduce Cu(II) ions into a MOF-based heterojunction to construct a signal-switchable PEC platform. Water-stable Zr-MOF and TiO_2 nanorods (NRs) could be assembled to prepare a "Z-scheme" Zr-MOF@TiO_2 NRs electrode via a solvothermal method. Cu(II) ions are selected to modulate the photocurrent of the Zr-MOF@TiO_2 NRs and serve as the recognition elements. The overlaps between the excitation spectrum of Zr-MOF and the absorption spectrum of Cu(II) ions are expected to cause a competitive absorption effect, and the resulting ineffective excitation of Zr-MOF@TiO_2 NRs suppresses the photocurrent. As shown in Scheme 1, zeolitic imidazolate framework-8 nanoparticles (ZIF-8 NMOFs) are used as a nanocarrier to conjugate ALP and the secondary antibody (mAb_2) to form an ALP/mAb_2 conjugating ZIF-8 NMOFs complex (ZIF-8@ALP-mAb_2) for the cTnI PEC immunoassay. After forming a sandwich immunocomplex in 96-well plates in the presence of cTnI targets, H_2S can be generated from sodium thiophosphate (Na_3SPO_3) by the confined ALP. When enzymatically generated H_2S reacts with Cu(II) ions to immediately form stable CuS, the competitive absorption of Cu(II) ions was switched from the on-state (Cu^{2+}@Zr-MOF@TiO_2 NRs) to the off-state (CuS@Zr-MOF@TiO_2 NRs). Under this condition, the greater negative potential of the CuS conduction band (CB) in the newly formed charge-carrier migration pathway enhances the signal-on photocurrent. Hence, a cTnI-dependent immunoreaction manifests as an enhanced photocurrent. This proof-of-concept study demonstrates the application of competitive absorption in a MOF-based heterostructure for PEC immunoassays.

EXPERIMENTAL SECTION

Synthesis of the Cu^{2+}@Zr-MOF@TiO_2 NRs Photoelectrode. The Zr-MOF@TiO_2 NRs electrode was prepared by a solvothermal method (see in the Supporting Information).[31] Cu^{2+}@Zr-MOF@TiO_2 NRs were synthesized via post-synthetic modification (PSM) of the Zr-MOF@TiO_2 NRs electrode with Cu(II) ions.[32,33] In a typical synthesis process, the Zr-MOF@TiO_2 NRs electrode was immersed in a $Cu(NO_3)_2$ solution (0.1 M) and heated at 60 °C for 24 h. The final product was rinsed with ultrapure water three times, and acetone was used to exchange the residual organic material before drying under vacuum at 70 °C for 2 h.

Immunoassay Protocol. The primary antibody (mAb_1, 20 μL, 0.25 mg/mL) was added to each well of a 96-well microplate and incubated at 4 °C for >12 h. Excess mAb_1 was

https://doi.org/10.1021/acs.analchem.2c03263
Anal. Chem. 2022, 94, 13582−13589

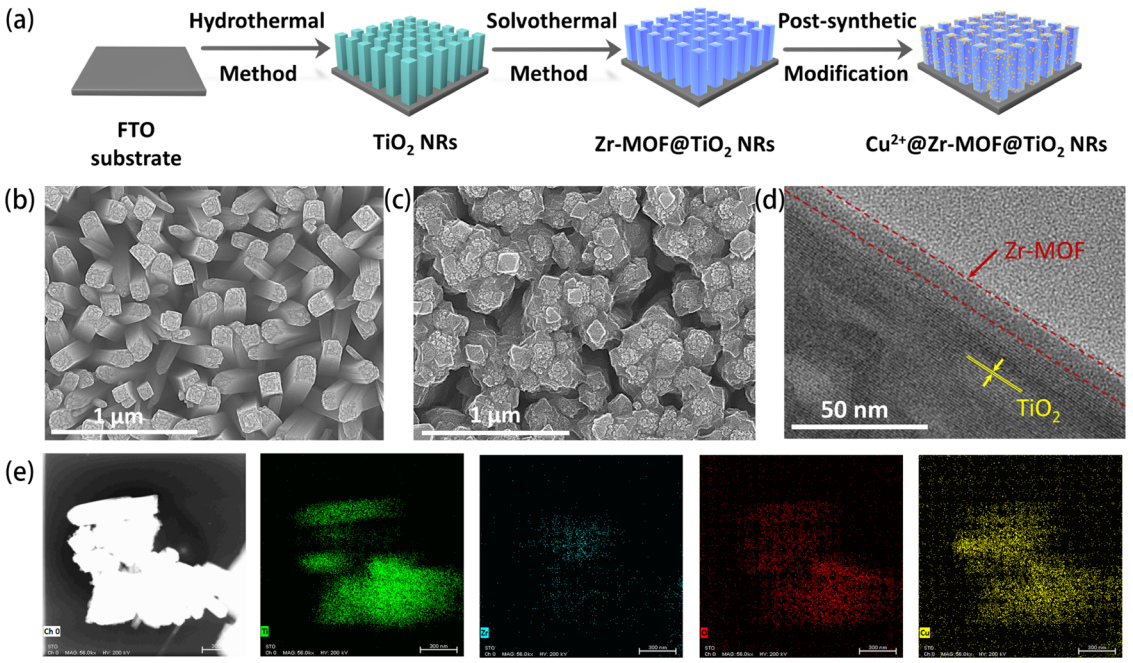

Figure 1. Synthesis and spectroscopic characterization of the Cu^{2+}@Zr-MOF@TiO_2 NRs photoelectrode: (a) schematic of the synthesis protocol; (b, c) SEM images of TiO_2 NRs and Zr-MOF@TiO_2 NRs; (d) TEM image of Zr-MOF@TiO_2 NRs; (e) and the corresponding elemental maps showing the distribution of Ti, Zr, O, and Cu in Cu^{2+}@Zr-MOF@TiO_2 NRs.

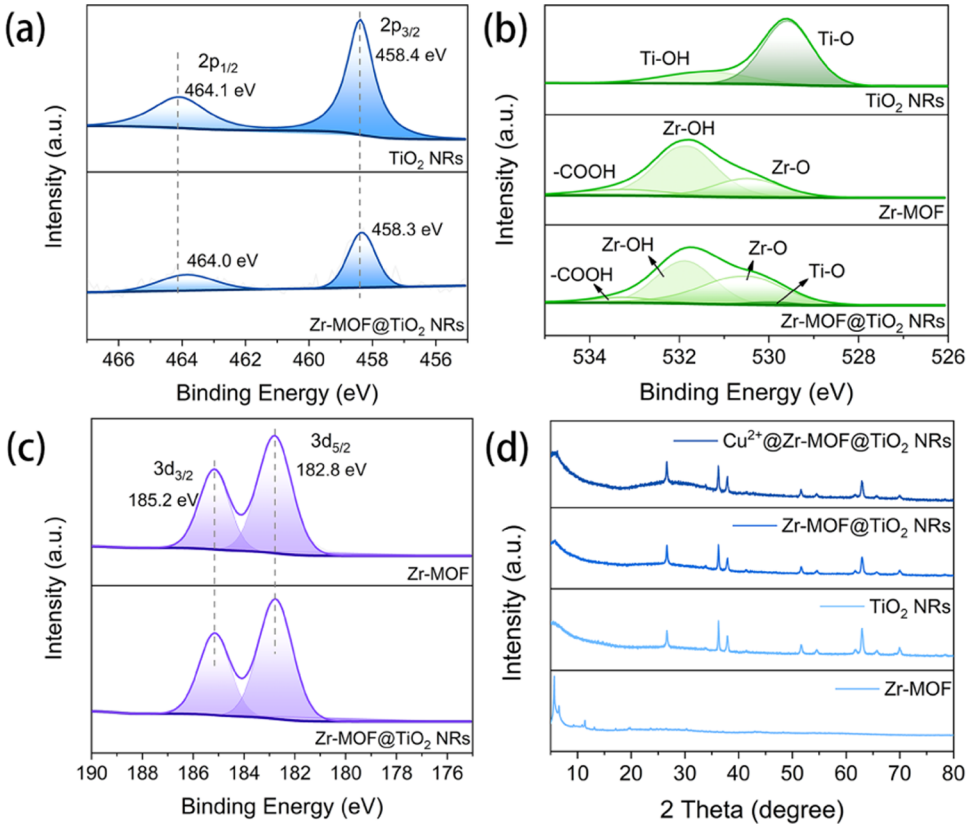

Figure 2. Bonding states and crystal structures of Zr-MOF, TiO_2 NRs, Zr-MOF@TiO_2 NRs, and Cu^{2+}@Zr-MOF@TiO_2 NRs obtained by XPS and XRD: (a–c) high-resolution XPS spectra of the Ti 2p, O 1s, and Zr 3d peaks and (d) XRD patterns.

removed with 10 mM phosphate-buffered saline (PBS, pH 7.4) containing 0.05% Tween 20. Bovine serum albumin (BSA) blocking buffer (40 μL, 3%) was added and incubated at 4 °C to occlude the nonspecific binding sites, followed by a flushing procedure. cTnI antigen solutions (40 μL) of different concentrations were sequentially added to each well and incubated at 37 °C for 1 h. Excess cTnI antigens were removed by PBS washing buffer prior to bioconjugation with ZIF-8@

https://doi.org/10.1021/acs.analchem.2c03263
Anal. Chem. 2022, 94, 13582−13589

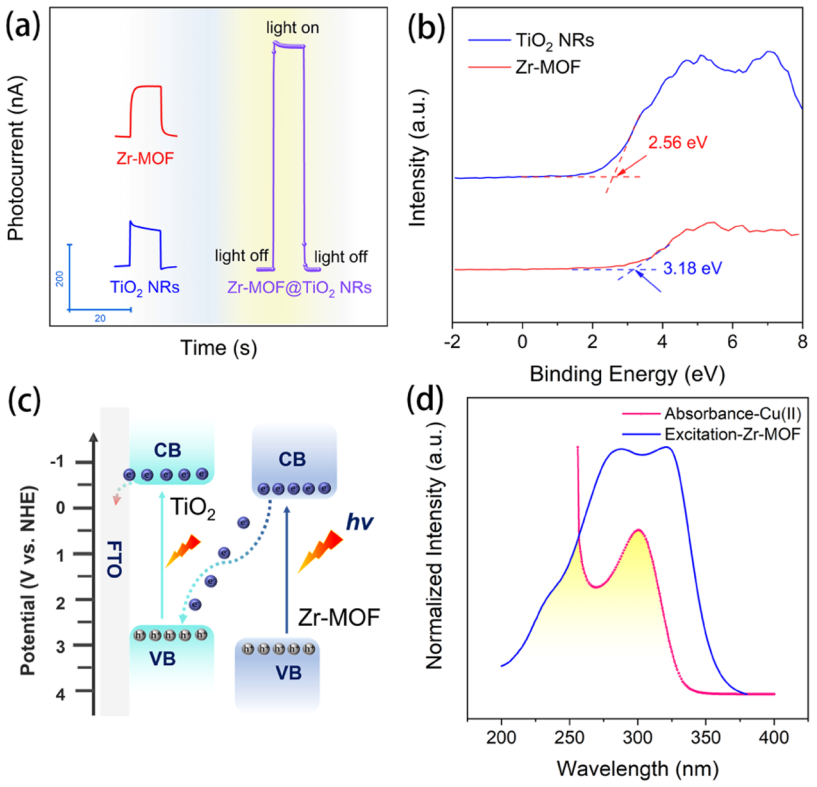

Figure 3. Charge transfer mechanism in Zr-MOF@TiO_2 NRs and the competitive absorption effect in Cu^{2+}@Zr-MOF@TiO_2 NR: (a) PEC response of Zr-MOF, TiO_2 NRs, and Zr-MOF@TiO_2 NRs heterojunction; (b) VB XPS analysis of Zr-MOF and TiO_2 NRs; (c) proposed charge transfer pathway in the Zr-MOF@TiO_2 NR heterojunction; and (d) competitive absorption effect in Cu^{2+}@Zr-MOF@TiO_2 NRs demonstrated by the overlapping normalized UV−vis absorption and fluorescence excitation spectra of Cu(II) ions and Zr-MOF.

ALP-mAb_2 (30 μL; see in the Supporting Information) at 37 °C for 1 h. After washing with Tris-HCl buffer (0.1 M, pH 8.8), Na_3SPO_3 (30 μL, 1 mM in Tris-HCl buffer) was added, and the mixture was incubated at 37 °C for 1.5 h to give the biocatalytic reaction solution. Finally, the reaction solution was transferred onto the surface of the Cu^{2+}@Zr-MOF@TiO_2 NRs electrode for PEC biosensing associated with the cTnI antigens.

RESULTS AND DISCUSSION

Characterization of Materials. The PEC biosensor was fabricated on a TiO_2 NRs supporting photoelectrode (Figure 1a) using sequential in situ growth of Zr-MOF and loading of Cu(II) ions. TiO_2 NRs on a fluorine-doped tin oxide (FTO) substrate were prepared via a hydrothermal method according to the reported literature,[34] and their morphology was examined by scanning electron microscopy (SEM). The as-synthesized TiO_2 NRs revealed a nearly perpendicular nanorod array structure and a smooth wall (Figure 1b). After decoration with Zr-MOF, the exposed surface of the TiO_2 NRs was completely covered by the MOF (Figure 1c). Examination of the Zr-MOF@TiO_2 NRs by transmission electron microscopy (TEM) showed that the TiO_2 NRs were crystallized with a lattice spacing of 0.324 nm, which corresponded to the (110) lattice plane of TiO_2 (Figure 1d). The evident division (labeled in red) between the Zr-MOF layer (thickness ≈ 12 nm) and TiO_2 NRs indicated intimate contact. The ζ potential of Zr-MOF (∼ −20 mV; Figure S1) suggested that loading of the positively charged Cu(II) ions onto the negatively charged Zr-MOF@TiO_2 NRs to form the Cu^{2+}@Zr-MOF@TiO_2 NRs was electrostatically favored. Energy-dispersive X-ray spectroscopy mapping images of Cu^{2+}@Zr-MOF@TiO_2 NRs (Figure 1e) showed that Ti, Zr, O, and Cu were evenly distributed on the sample, indicating successful construction of the photoelectrode.

The bonding states of the Zr-MOF@TiO_2 NRs heterojunction were investigated by X-ray photoelectron spectroscopy (XPS) using Zr-MOF and TiO_2 NRs as reference samples. The XPS survey spectrum of Zr-MOF@TiO_2 NRs confirmed the coexistence of Ti, O, and Zr (Figure S2). The high-resolution XPS spectra of Ti (Figure 2a) revealed binding energies at 464.1 and 458.4 eV, which were ascribed to Ti $2p_{1/2}$ and Ti $2p_{3/2}$ orbitals in the TiO_2 NRs, respectively, implying the existence of normal Ti^{4+}.[35] After coating with Zr-MOF, the binding energies of Ti exhibited a negative shift of ∼0.1 eV relative to TiO_2 NRs. This agreed with the effective coupling between Ti and the Zr-MOF involving electron transfer from the ligand to the metal atom at their combination interface. The peaks centered at 531.5 and 529.5 eV were assigned to adsorbed −OH and Ti−O bonds in the TiO_2 NRs (Figure 2b). The O 1s peaks of Zr-MOF at 533.5 and 530.4 eV agreed with −COOH and Zr−O−Zr, respectively. Consequently, the O 1s of Zr-MOF@TiO_2 NRs could be separated into four peaks corresponding to TiO_2 and Zr-MOF. Although peaks due to adsorbed −OH were present in the XPS spectra of TiO_2 (Ti−OH) and Zr-MOF (Zr−OH), it was more reasonable to assume that the corresponding peak in Zr-MOF@TiO_2 NRs was attributed to the Zr-MOF layer rather than the TiO_2 substrate. These results supported the successful preparation of the Zr-MOF@TiO_2 NRs heterojunction. The XPS Zr 3d peaks at 185.2 and 182.8 eV (Figure 2c) were indexed to Zr $3d_{3/2}$ and Zr $3d_{5/2}$ in Zr-MOF, respectively, and

https://doi.org/10.1021/acs.analchem.2c03263
Anal. Chem. 2022, 94, 13582−13589

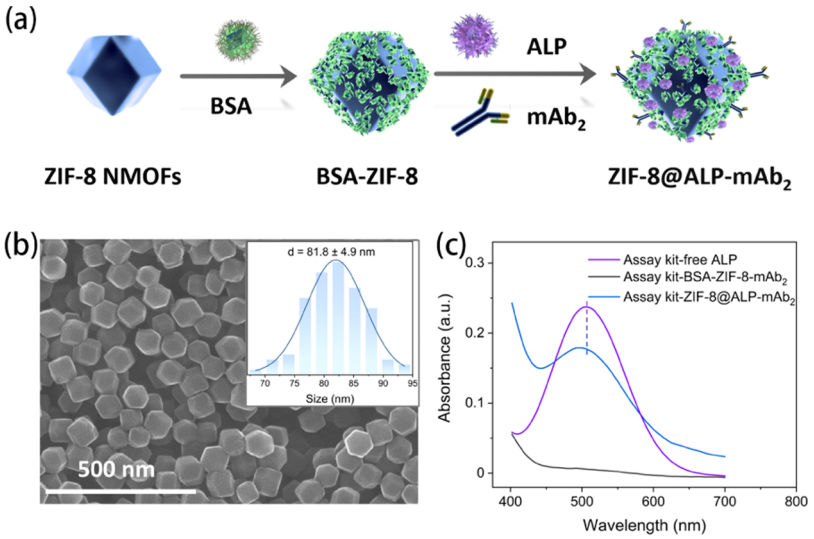

Figure 4. Characterization of ZIF-8@ALP-mAb_2: (a) schematic diagram of the synthesis process; (b) SEM image of ZIF-8 NMOFs (inset histogram shows the corresponding size distributions); and (c) UV−vis absorption spectra showing the responses of the ALP activity assay kit to free ALP, BSA-ZIF-8-mAb_2, and ZIF-8@ALP-mAb_2.

no visible difference in binding energies was observed in Zr-MOF@TiO_2 NRs. The X-ray diffraction (XRD) patterns of Zr-MOF, TiO_2 NRs, Zr-MOF@TiO_2 NRs, and Cu^{2+}@Zr-MOF@TiO_2 NRs are shown in Figure 2d. Zr-MOF@TiO_2 NRs displayed diffraction peak characteristics of TiO_2 and Zr-MOF, which supported the successful in situ growth of a thin Zr-MOF layer on the surface of the TiO_2 NRs. The diffraction pattern obtained from Cu^{2+}@Zr-MOF@TiO_2 NRs was also similar to that of Zr-MOF@TiO_2 NRs, demonstrating that the crystal structure of heterojunction was retained after PSM treatment with Cu(II) ions.

Mechanism of Charge Transfer in Zr-MOF@TiO_2 NRs. To confirm the enhanced photoelectric response of the heterojunction, the PEC activity of Zr-MOF@TiO_2 NRs was compared with that of the parent Zr-MOF and TiO_2 NRs. Figure 3a illustrates that compared with the photocurrents of TiO_2 NRs (~115 nA) and Zr-MOF (~152 nA), the signal obtained from Zr-MOF@TiO_2 NRs attained 680 nA. This indicated the heterojunction formed by coupling Zr-MOF and TiO_2 NRs inhibited the recombination of photogenerated electron−hole pairs, thereby enhancing the photoelectric conversion efficiency. UV−vis diffuse reflectance spectra (UV−vis DRS) and valence band (VB) XPS spectra were used to study the electronic states of Zr-MOF and TiO_2 NRs. As shown in Figure S3, the abrupt onsets of isolated Zr-MOF and TiO_2 NRs were approximately 360 and 405 nm, respectively. From this, their energy band gaps (E_g) were calculated to be 3.46 and 3.06 eV, respectively. Figure 3b shows that the VB potentials of Zr-MOF and TiO_2 NRs were ~3.18 and 2.56 eV, respectively. Based on these results, the corresponding conduction bands of Zr-MOF and TiO_2 NRs were estimated to be −0.28 and −0.5 eV, respectively. A proposed charge transfer pathway in the Zr-MOF@TiO_2 NR heterojunction is depicted in the schematic energy level diagram of Figure 3c. The scheme shows that when Zr-MOF@TiO_2 NRs are excited, spontaneous migration of photogenerated electrons from the CB of Zr-MOF to the VB of TiO_2 occurs at the contact interface. Hence, a direct Z-scheme heterojunction is formed, which agrees with studies elsewhere.[36] Because the TiO_2 NRs are in direct contact with the surface of FTO, the photogenerated electron transfer pathway from outer shell Zr-MOF to inner TiO_2 NRs is feasible, as evidenced by the improved photocurrent signal of Zr-MOF@TiO_2 NRs.

Competitive Absorption Effect in Cu^{2+}@Zr-MOF@TiO_2 NRs. The photoluminescence properties of MOFs are reported to be closely related to their corresponding ligands.[37,38] The fluorescence excitation spectrum of the ligand (H_2Bpdc) in Zr-MOF (broad band centered at 200−380 nm; Figure S4) was similar to the fluorescence spectrum of Zr-MOF (Figure S5). The normalized UV−vis absorption and fluorescence excitation spectra of Cu(II) ions and Zr-MOF revealed an overlap in the wavelength range between 200 and 340 nm (Figure 3d). The results implied that the absorption of light by Cu(II) ions in Cu^{2+}@Zr-MOF@TiO_2 NRs limits the available light energy for the excitation of Zr-MOF, resulting in inefficient excitation and a decreased photocurrent. Consequently, the Cu^{2+}@Zr-MOF@TiO_2 NRs photoelectrode exhibited a low background and stable signal output (Figure S6), which is beneficial for PEC sensing.

Characterization of ZIF-8@ALP-mAb_2. The procedure used to construct ZIF-8@ALP-mAb_2 is illustrated in Figure 4a. ZIF-8 NMOFs were synthesized from 2-methylimidazole and zinc acetate, and their surface was modified with bovine serum albumin (BSA) by electrostatic interaction to obtain BSA-modified ZIF-8 NMOFs (BSA-ZIF-8). The introduction of BSA provided abundant amino sites to anchor mAb_2 and ALP by the formation of amide bonds. The large surface area of the ZIF-8 NMOFs carrier maximized ALP loading to achieve effective signal amplification for PEC biosensing. The SEM image of ZIF-8 NMOFs (Figure 4b) showed a rhombic dodecahedral morphology with an average diameter of ~81.8 nm. The XRD pattern (Figure S7) corresponded to planes (011), (002), (112), (022), (013), and (222), which agreed with high-purity ZIF-8.[39,40] The ALP activity assay kit was used to verify the catalytic activities of free ALP, BSA-ZIF-8-labeled on mAb_2 (BSA-ZIF-8-mAb_2), and ZIF-8@ALP-mAb_2; ALP interacts with substrates to generate new species, which can be detected by monitoring the absorption at 510 nm. The UV−vis absorption spectra exhibited strong absorption peaks

https://doi.org/10.1021/acs.analchem.2c03263
Anal. Chem. 2022, 94, 13582−13589

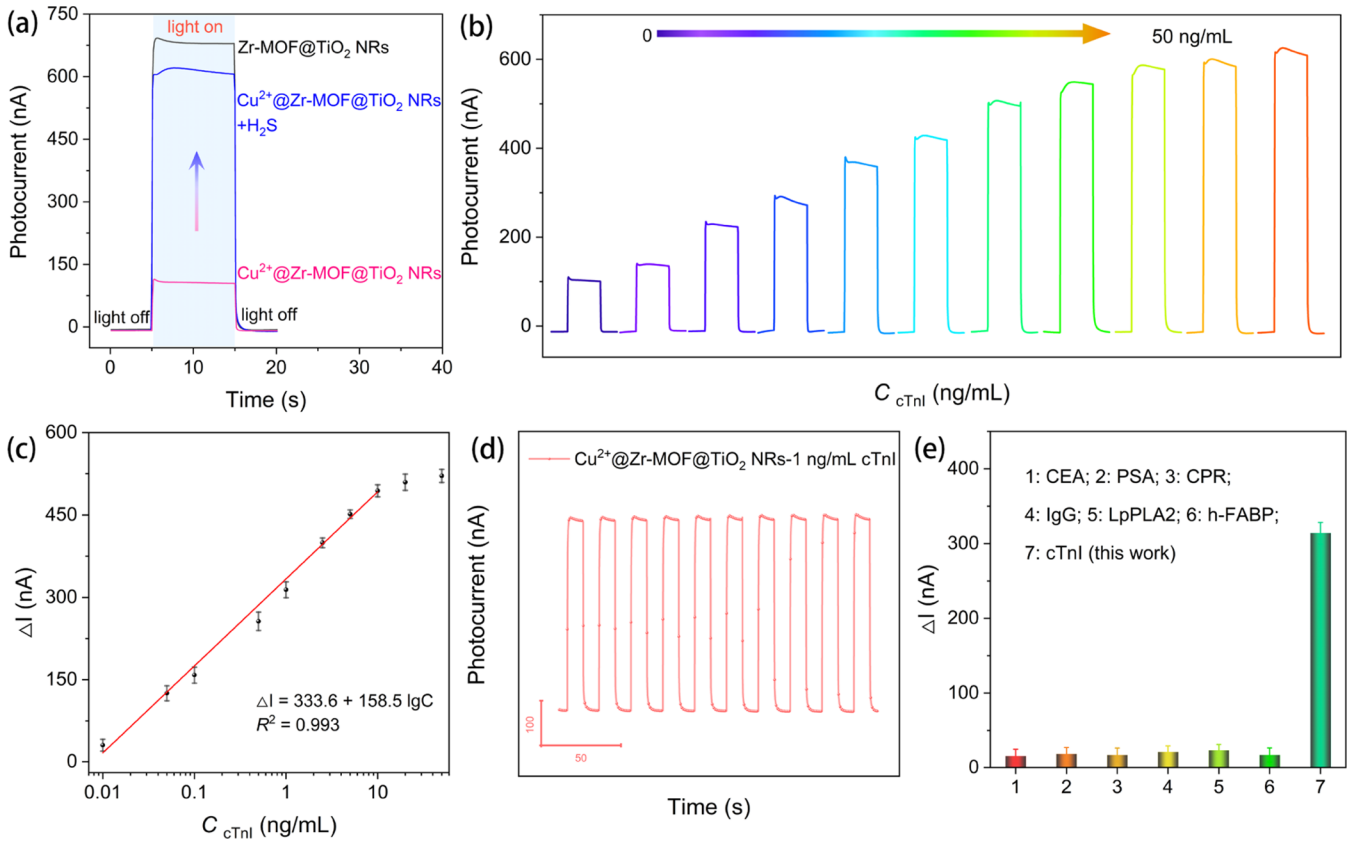

Figure 5. Development and performance of the PEC biosensor: (a) photocurrent responses of Zr-MOF@TiO_2 NRs and Cu^{2+}@Zr-MOF@TiO_2 NRs before and after the reaction with H_2S; (b) changes in Cu^{2+}@Zr-MOF@TiO_2 NR PEC biosensor photocurrent signals in response to the increasing concentrations of the cTnI antigen; (c) calibration curve for the detection of cTnI derived from (ΔI) and the logarithm of cTnI concentrations over 0.01−10 ng/mL; (d) operational stability of Cu^{2+}@Zr-MOF@TiO_2 NRs at 1 ng/mL cTnI over 200 s; and (e) selectivity of the PEC biosensor toward cTnI. Photocurrent tests were performed in 4-(2-hydroxyethyl)-1-piperazineethanesulfonic acid buffer (10 mM, pH 7.4).

for ALP and ZIF-8@ALP-mAb_2 (Figure 4c), suggesting that the catalytic activity of ALP was retained after loading onto the MOF. In contrast, BSA-ZIF-8-mAb_2 gave no response (510 nm) with the assay kit.

Development of the PEC Sensing Platform. Figure 5a shows how the photocurrent of the Zr-MOF@TiO_2 NRs electrode (680 nA) decreased after loading Cu(II) ions onto its architecture (Cu^{2+}@Zr-MOF@TiO_2 NR, 116 nA) due to the competitive absorption between Cu(II) ions and Zr-MOF. Under this condition, the Cu(II) ions in Cu^{2+}@Zr-MOF@TiO_2 NRs were defined as existing in the on-state. After incubation with H_2S, the photocurrent of the PEC increased by a factor of about 5 compared with pristine Cu^{2+}@Zr-MOF@TiO_2. This phenomenon can be attributed to the fact that the formation of CuS nullified the competitive absorption effect of Cu(II) ions, in which Cu(II) ions in the newly formed CuS@Zr-MOF@TiO_2 NRs were defined as existing in the off-state. The increased photoelectric efficiency of CuS@Zr-MOF@TiO_2 NRs could also be attributed to the greater negative potential of the CuS CB in the newly formed charge-carrier migration pathway. Hence, the combined synergistic effects constituted a sensitive signal-on platform to construct PEC biosensors.

Performance of the Cu^{2+}@Zr-MOF@TiO_2 NRs PEC Biosensor. After sandwich immunorecognition in a 96-well plate, the confined ALP on the ZIF-8 NMOFs catalyzed the generation of H_2S from Na_3SPO_3. Hence, the target-dependent reaction between Cu(II) ions and H_2S in the PEC immunosensor was applied to the detection of cTnI. Figure 5b shows that the photocurrent of Cu^{2+}@Zr-MOF@TiO_2 NRs increased with increasing concentrations of cTnI from 0.01 to 50 ng/mL. A linear correlation was obtained between the difference in photocurrents (ΔI) before and after exposure to cTnI and the logarithm of the cTnI concentrations over 0.01−10 ng/mL (R^2 = 0.993, n = 8; Figure 5c). The limit of detection (8.6 pg/mL; S/N = 3) demonstrated high sensitivity toward cTnI and was compared favorably with other detection methods (Table S1). The photocurrents obtained from repeated on/off illumination measurements with 1 ng/mL cTnI over 200 s showed no deterioration in the signal (Figure 5d), indicating good operational stability. Five independent PEC/cTnI biosensors were used to assay 1 ng/mL cTnI under the same experimental conditions, and the relative standard deviation (RSD) was calculated to be 5.3% (Figure S8), indicating satisfactory reproducibility. The reported demarcation concentration of cTnI, distinguishing healthy people from those at risk of AMI, ranges from 0.5 to 2.0 ng/mL; levels of cTnI can reach 50 ng/mL in AMI patients.[41] These values were within the operational range of the PEC biosensor, confirming its suitability for cTnI monitoring.

The selectivity of the Cu^{2+}@Zr-MOF@TiO_2 NRs was evaluated by challenging the PEC/cTnI detection system with relevant interferent proteins (i.e., carcinoembryonic antigen (CEA), prostate-specific antigen (PSA), C-reactive protein (CRP), immunoglobulin G (IgG), lipoprotein-associated phosphohpaseA2 (LpPLA2), and h-FABP). Despite a 10-fold

https://doi.org/10.1021/acs.analchem.2c03263
Anal. Chem. 2022, 94, 13582−13589

excess of interferents relative to the cTnI target (1 ng/mL), negligible variation in photocurrents was recorded under the same test conditions (Figure 5e), illustrating the high selectivity of the Cu^{2+}@Zr-MOF@TiO_2 NRs immunosensor toward cTnI.

Analysis of Real Samples. For evaluating the accuracy of the Cu^{2+}@Zr-MOF@TiO_2 NRs PEC/cTnI system in the complex physiological environment, the developed photoelectrode was applied to test seven human serum samples, obtained from the local hospital. These serum samples were centrifuged for 10 min at 6000*g* to remove the possible precipitate. After the pretreatment process, the same serum sample was detected with two analytic methods: the PEC/cTnI system and a commercial human cTnI ELISA kit. The results from Table S2 showed good consistency between our PEC biosensor and ELISA, which exhibited acceptable accuracy for the detection in real samples using our PEC/cTnI system.

CONCLUSIONS

A highly sensitive and tunable competitive absorption-induced signal-on PEC immunoassay was developed for cTnI detection. Cu^{2+}@Zr-MOF@TiO_2 NRs were prepared by sequential hydrothermal, solvothermal, and postsynthetic methods. A competitive absorption effect, arising from the loading of Cu(II) ions onto a Zr-MOF@TiO_2 NRs Z-scheme heterojunction suppressed the PEC background signal and provided the recognition element for target-dependent H_2S generated by the immune recognition-confined ALP. After responding to H_2S, the newly formed CuS@Zr-MOF@TiO_2 NRs photoelectrode exhibited significant signal enhancement due to the weakened competitive absorption effect and increased efficiency of the electron transfer path associated with CuS. The Cu^{2+}@Zr-MOF@TiO_2 NR PEC biosensor demonstrated high sensitivity and selectivity toward cTnI detection. This work provides a new strategy for PEC biosensing based on the competitive absorption effect in modulated MOF Z-scheme heterojunctions.

ASSOCIATED CONTENT

Supporting Information

The Supporting Information is available free of charge at https://pubs.acs.org/doi/10.1021/acs.analchem.2c03263.

Reagents and materials; instruments; synthesis of the TiO_2 NRs electrode; synthesis of the Zr-MOF@TiO_2 NRs electrode; preparation of ZIF-8@ALP-mAb$_2$; ζ potential of Zr-MOF; XPS survey spectra of samples; UV−vis DRS and corresponding plots of $(Ah\nu)^2$ versus energy ($h\nu$); fluorescence spectra of the H_2Bpdc ligand and Zr-MOF; operational stability of the Cu^{2+}@Zr-MOF@TiO_2 NRs electrode; XRD pattern of ZIF-8 NMOFs; comparison of various methods for cTnI detection; and comparison of the assayed results using the PEC/cTnI detection biosensor and the commercial cTnI ELISA kit (PDF)

AUTHOR INFORMATION

Corresponding Authors

Meijin Li − *Key Laboratory of Analytical Science for Food Safety and Biology (MOE & Fujian Province), Department of Chemistry, Fuzhou University, Fuzhou 350108, People's Republic of China;* orcid.org/0000-0002-8245-5556; Phone: +86-591-2286 6125; Email: mjli@fzu.edu.cn; Fax: +86-591-2286 6135

Dianping Tang − *Key Laboratory of Analytical Science for Food Safety and Biology (MOE & Fujian Province), Department of Chemistry, Fuzhou University, Fuzhou 350108, People's Republic of China;* orcid.org/0000-0002-0134-3983; Phone: +86-591-2286 6125; Email: dianping.tang@fzu.edu.cn; Fax: +86-591-2286 6135

Authors

Yuan Gao − *Key Laboratory of Analytical Science for Food Safety and Biology (MOE & Fujian Province), Department of Chemistry, Fuzhou University, Fuzhou 350108, People's Republic of China*

Yongyi Zeng − *The United Innovation of Mengchao Hepatobiliary Technology Key Laboratory of Fujian Province, Mengchao Hepatobiliary Hospital of Fujian Medical University, Fuzhou 350025, People's Republic of China*

Xiaolong Liu − *The United Innovation of Mengchao Hepatobiliary Technology Key Laboratory of Fujian Province, Mengchao Hepatobiliary Hospital of Fujian Medical University, Fuzhou 350025, People's Republic of China;* orcid.org/0000-0002-3096-4981

Complete contact information is available at: https://pubs.acs.org/10.1021/acs.analchem.2c03263

Notes

The authors declare no competing financial interest.

ACKNOWLEDGMENTS

The authors gratefully acknowledge the financial support from the National Natural Science Foundation of China (Grant Nos. 21874022 and 21675029).

REFERENCES

(1) Lin, Y.-T.; Wang, L.; Cheng, Y.; Lee, C.; Tsai, H. *ACS Sens.* **2021**, *6*, 2429−2435.

(2) Chen, F.-Z.; Li, Z.; Liu, X.; Zhu, Y.; Han, D.; Chen, H. *Anal. Chem.* **2021**, *93*, 5001−5004.

(3) Ouyang, M.; Tu, D.; Tong, L.; Sarwar, M.; Bhimaraj, A.; Li, C.; Coté, G.; Di Carlo, D. *Biosens. Bioelectron.* **2021**, *171*, No. 112621.

(4) Shi, Z.; Xu, Z.; Hu, J.; Wei, W.; Zeng, X.; Zhao, W.; Lin, P. *Biosens. Bioelectron.* **2022**, *201*, No. 113958.

(5) Chen, F.-Z.; Han, D.; Chen, H. *Anal. Chem.* **2020**, *92*, 8450−8458.

(6) Wang, J.; Jiang, C.; Jin, J.; Huang, L.; Yu, W.; Su, B.; Hu, J. *Angew. Chem., Int. Ed.* **2021**, *60*, 13042−13049.

(7) Wang, Y.-T.; Wu, N.; Yang, T.; Wang, J. *Anal. Chem.* **2020**, *92*, 5540−5545.

(8) Li, F.; Zhao, A.; Li, Z.; Xi, Y.; Jiang, J.; He, J.; Wang, J.; Cui, H. *Anal. Chem.* **2022**, *94*, 2665−2675.

(9) Yu, Z.; Gong, H.; Xu, J.; Li, Y.; Xue, F.; Zeng, Y.; Liu, X.; Tang, D. *Anal. Chem.* **2022**, *94*, 7408−7416.

(10) Yu, Z.; Gong, H.; Gao, Y.; Li, L.; Xue, F.; Zeng, Y.; Li, M.; Liu, X.; Tang, D. *Small* **2022**, *18*, No. 2202564.

(11) Feng, S.; Yan, M.; Xue, Y.; Huang, J.; Yang, X. *Anal. Chem.* **2021**, *93*, 13572−13579.

(12) Gao, Y.; Zeng, Y.; Liu, X.; Tang, D. *Anal. Chem.* **2022**, *94*, 4859−4865.

(13) Zhu, Y.-C.; Li, Z.; Liu, X.; Fan, G.; Han, D.; Zhang, P.; Zhao, W.; Xu, J.; Chen, H. *Biosens. Bioelectron.* **2020**, *148*, No. 111836.

(14) Zeng, R.; Xu, J.; Lu, L.; Lin, Q.; Huang, X.; Huang, L.; Li, M.; Tang, D. *Chem. Commun.* **2022**, *58*, 7562−7565.

(15) Zeng, R.; Gong, H.; Li, Y.; Li, Y.; Lin, W.; Tang, D.; Knopp, D. *Anal. Chem.* **2022**, *94*, 7442−7448.
(16) Li, Y.; Zeng, R.; Wang, W.; Xu, J.; Gong, H.; Li, L.; Li, M.; Tang, D. *ACS Sens.* **2022**, *7*, 1593−1601.
(17) Al Danaf, N.; Schrimpf, W.; Hirschle, P.; Lamb, D.; Ji, Z.; Wuttke, S. *J. Am. Chem. Soc.* **2021**, *143*, 10541−10546.
(18) Cai, G.; Yan, P.; Zhang, L.; Zhou, H.; Jiang, H. *Chem. Rev.* **2021**, *121*, 12278−12326.
(19) Zhan, W.-w.; Kuang, Q.; Zhou, J.; Kong, X.; Xie, Z.; Zheng, L. *J. Am. Chem. Soc.* **2013**, *135*, 1926−1933.
(20) Dong, W.; Li, Z.; Wen, W.; Liu, B.; Wen, G. *ACS Appl. Mater. Interfaces* **2021**, *13*, 57497−57504.
(21) Fu, Y.; Xiao, K.; Zhang, X.; Du, C.; Chen, J. *Anal. Chem.* **2021**, *93*, 1076−1083.
(22) Chen, F.-Z.; Gao, Y.; Li, Y.; Li, W.; Wu, X.; Han, D.; Zhao, W. *Sens. Actuators, B* **2022**, *361*, No. 131651.
(23) Hang, T.; Li, C.; Liang, D.; Li, S.; Zhou, H.; Ge, P.; Zhu, X.; Liu, T. *Chem. Eng. J.* **2022**, *431*, No. 133465.
(24) Zhang, X.; Yan, T.; Wu, T.; Feng, Y.; Sun, M.; Yan, L.; Du, B.; Wei, Q. *Biosens. Bioelectron.* **2019**, *135*, 88−94.
(25) Wu, T.; Yan, T.; Zhang, X.; Feng, Y.; Wei, D.; Sun, M.; Du, B.; Wei, Q. *Biosens. Bioelectron.* **2018**, *117*, 575−582.
(26) Zhang, Q.; Liu, S.; Du, C.; Fu, Y.; Xiao, K.; Zhang, X.; Chen, J. *Anal. Chem.* **2021**, *93*, 14272−14279.
(27) Zhao, Y.; Zeng, H.; Zhu, X.; Lu, W.; Li, D. *Chem. Soc. Rev.* **2021**, *50*, 4484−4513.
(28) Xu, H.; Gao, J.; Qian, X.; Wang, J.; He, H.; Cui, Y.; Yang, Y.; Wang, Z.; Qian, G. *J. Mater. Chem. A* **2016**, *4*, 10900−10905.
(29) Xu, J.; Zhang, H.; Zhang, W.; Li, P.; Zhang, W.; Wang, H.; Tang, B. *Chem. Commun.* **2020**, *56*, 2431−2434.
(30) Zhou, Q.; Li, G.; Chen, K.; Yang, H.; Yang, M.; Zhang, Y.; Wan, Y.; Shen, Y.; Zhang, Y. *Anal. Chem.* **2020**, *92*, 983−990.
(31) Zhu, X.; Li, B.; Yang, J.; Li, Y.; Zhao, W.; Shi, J.; Gu, J. *ACS Appl. Mater. Interfaces* **2015**, *7*, 223−231.
(32) Han, X.; Gu, C.; Ding, Y.; Yu, J.; Li, K.; Zhao, D.; Chen, B. *ACS Appl. Mater. Interfaces* **2021**, *13*, 20371−20379.
(33) Zhang, X.; Hu, Q.; Xia, T.; Zhang, J.; Yang, Y.; Cui, Y.; Chen, B.; Qian, G. *ACS Appl. Mater. Interfaces* **2016**, *8*, 32259−32265.
(34) Luo, L.; Chen, W.; Xu, S.; Yang, J.; Li, M.; Zhou, H.; Xu, M.; Shao, M.; Kong, X.; Li, Z.; Duan, H. *J. Am. Chem. Soc.* **2022**, *144*, 7720−7730.
(35) Tang, R.; Zhou, S.; Yuan, Z.; Yin, L. *Adv. Funct. Mater.* **2017**, *27*, No. 1701102.
(36) Wang, X.; Sun, W.; Tian, Y.; Dang, K.; Zhang, Q.; Shen, Z.; Zhan, S. *Small* **2021**, *17*, No. 2100367.
(37) Perego, J.; Bezuidenhout, C.; Villa, I.; Cova, F.; Crapanzano, R.; Frank, I.; Pagano, F.; Kratochwill, N.; Auffray, E.; Bracco, S.; Vedda, A.; Dujardin, C.; Sozzani, P.; Meinardi, F.; Comotti, A.; Monguzzi, A. *Nat. Commun.* **2022**, *13*, No. 3504.
(38) Sun, Y.-Q.; Cheng, Y.; Yin, X. *Anal. Chem.* **2021**, *93*, 3559−3566.
(39) Zhong, T.; Li, S.; Li, X.; JiYe, Y.; Mo, Y.; Chen, L.; Zhang, Z.; Wu, H.; Li, M.; Luo, Q. *Food Chem.* **2022**, *384*, No. 132495.
(40) Gao, Y.; Wu, J.; Wang, J.; Fan, Y.; Zhang, S.; Dai, W. *ACS Appl. Mater. Interfaces* **2020**, *12*, 11036−11044.
(41) Han, X.; Li, S.; Peng, Z.; Othman, A.; Leblanc, R. *ACS Sens.* **2016**, *1*, 106−114.

https://doi.org/10.1021/acs.analchem.2c03263
Anal. Chem. 2022, 94, 13582−13589